Controllable synthesis of porous and hollow nanostructured catalyst particles and their soot oxidation

*Duhaul Biqal Kautsar, Phong Hoai Le, Ai Ando, Kiet Le Anh Cao, Eka Lutfi Septiani, Tomoyuki Hirano, and Takashi Ogi**

Chemical Engineering Program, Department of Advanced Science and Engineering, Graduate School of Advanced Science and Engineering, Hiroshima University, 1-4-1 Kagamiyama, Higashi-Hiroshima City, Hiroshima 739-8527, Japan

*Corresponding author: Takashi Ogi, ogit@hiroshima-u.ac.jp

Tel/Fax: +81-82-424-3765

KEYWORDS: three-way catalysts, macropore, nanostructured particles, spray process, self-assembly.

ABSTRACT

The introduction of macroporous structures into three-way catalysts (TWCs) through polymer template-assisted spray drying has attracted attention because of its enhanced gas diffusion and catalytic performance. However, the surface charge effect of polymeric template components has not been investigated to control the structure of TWC particles during synthesis. Thus, this study investigated the effect of template surface charges on the self-assembly behavior of TWC nanoparticles (NPs) during drying. The self-assembly of TWC NPs and polymer particles with different charges produced a hollow structure, whereas using the same charges generates a porous one. Consequently, the mechanism of particle self-assembly during drying and final structure particle formation is proposed in this study. Here, porous TWC particles demonstrated a faster oxidation of soot particles than hollow-structured particles. This occurred as a result of the larger contact area between the catalyst surface and solid reactant. Our findings propose a fundamental self-assembly mechanism for the formation of different TWC structures, thereby enhancing soot oxidation performance using macroporous structures.

INTRODUCTION

The development of submicron nanostructured particles with highly controlled structures and morphologies (e.g., porous,[1,2] hollow,[3,4] and core-shell[5,6]) is important for advancing the next generation of fine particles.[7–10] Among nanostructured particles, macroporous particles have attracted considerable attention due to their unique advantages in material performance. By introducing macropores, the particles can efficiently utilize their internal parts and concurrently improve their performance. For example, carbon particles with macroporous structures have been used as electrode materials in fuel cells.[11–14] Here, platinum nanoparticles (NPs) were supported in the macroporous structure, ensuring the high dispersion stability of platinum and improving electrocatalytic properties. Rahmatika et al. reported that silica particles with a macroporous structure can efficiently support cellulose nanofibers by generating exposed active surfaces in porous frameworks, thereby promoting efficient mass transportation in the liquid phase.[15,16] Our group reported that micron particles with macroporous structures using cellulose[17] and pectin[18] as building blocks can efficiently adsorb protein (such as lysozyme) from the liquid phase due to the easy penetration through macropores. The studies on macroporous structures across various materials and field applications have confirmed that the presence of macropores can enhance electrocatalytic performance and adsorption capacity.

The aforementioned concept has been recently applied to the field of environmental catalysts, particularly for three-way catalysts (TWCs) used in automotive exhaust systems to reduce emissions of three harmful pollutants: nitrogen oxides (NOx), carbon monoxide (CO), and hydrocarbons (HC). Generally, TWCs comprised Pd and Rh, which are anchored to the strong stabilizers, e.g., $CeZrO_4$ and Al_2O_3, making this material a promising candidate for converting these harmful gases into less harmful substances (e.g., CO_2, H_2O, and N_2). Our group successfully

synthesized macroporous structured particles using TWC NPs as building blocks through a polymer template-assisted spraying method.[19,20] The result confirmed that the presence of macropores improved the CO_2 adsorption rates compared with aggregate TWC particles. However, controlling the structure and morphology of TWC particles remains challenging. The important factors involved in controlling nanostructured particles are the particle size and surface charge properties of the template material.[21] To investigate the effect of template particle size on nanostructured particles, Le et al. synthesized macroporous TWC particles using various sizes of template poly(methyl methacrylate) (PMMA) particles (67–381 nm) through the spraying method.[22] As a result, macroporous TWC particles with different pore sizes were successfully synthesized, and the effect of pore size on macroporous TWC properties was experimentally clarified. However, for controlling the nanostructured particles using TWCs, the effect of the template surface charge on the particle structure has not been investigated so far.

To address the challenge of the structural control of TWC particles, this study focuses on investigating the effect of the surface charge of the template on the structure of TWC particles using the spray method. To the best of our knowledge, this is the first study to report the particle self-assembly mechanism. This study provides a deep understanding of the electrostatic interaction between the host (TWC particles) and template (PMMA particles) components that occurs during drying. Based on the self-assembly behavior of TWC and PMMA particles, the electrostatic forces (e.g., attraction or repulsion) were dependent on the surface charge of the precursor components. Here, negatively charged PMMA formed a hollow structure, whereas positively charged PMMA produced porous TWC particles after the experimental conditions were optimized. The pores and internal structure were evaluated to characterize the resulting particles. Furthermore, a preliminary

evaluation of the catalytic performance for CO and soot oxidation was conducted to compare the impact of the distinct structural features between hollow and porous TWC particles.

EXPERIMENTAL SECTION

Catalyst preparation

The precursor was prepared by mixing TWC NPs (average size = 8 nm; Mitsui Mining & Smelting Co., Ltd., Japan) and PMMA particles with a homogeneous spherical shape (Nippon Shokubai, Japan) in ultrapure water. Two surface charge types of PMMA were used. The first were negatively charged PMMA particles, obtained from commercial PMMA (334 nm). The second type included positively charged PMMA particles (average size = 368 nm) obtained via modification using cetyltrimethylammonium bromide (CTAB; ≥98%, Sigma-Aldrich, St. Louis, MO, USA). The surface charge modification of the PMMA particles is described in **Section 1** (Supporting Information). The morphologies and particle-size distributions of the TWC NPs and PMMA particles are shown in **Figure S2**. The precursor with a different composition shown in **Table 1** was fed into the spray pyrolysis apparatus. Based on the weight percentage of the precursor components, the number ratio of TWC NPs and PMMA particles is calculated and the detailed information is given in **Section 2** (Supporting Information). **Figure 1a** shows that the apparatus comprised an ultrasonic nebulizer for droplet production; a tubular furnace divided into four zones of 250°C, 350°C, 500°C, and 500°C; a bag filter with a temperature of 150°C where the sample was collected; and a water trap. N_2 (pressure, 0.1 MPa; flowing rate, 5 L/min) was used as the inert carrier gas to transport the droplets through the tubular furnace. The obtained particles were reheated in two steps using a horizontal furnace (**Figure 1b**). The first reheating step was performed at 900°C, with an increasing temperature rate of 5°C/min in N_2 at a gas flow rate of 1 L/min for 1 h. During the second reheating step, the particles were heated in air at 900°C, with an

increasing temperature rate of 5°C/min and a gas flow rate of 1 L/min for 4 h. The characteristics and catalytic performance of the final particles were subsequently analyzed.

Table 1. Synthesis conditions for the nanostructured TWC particles.

Sample name	[a]Zeta potential PMMA [mV]	PMMA and TWC ratio [wt%/wt%]	Reheating gas	
			First step	Second step
TNP1.0	−43.1 ± 1.2	1.0	-	-
TPP1.0	+53.9 ± 0.6	1.0	-	-
TNP1.0-N_2	−43.1 ± 1.2	1.0	N_2	-
TPP1.0-N_2	+53.9 ± 0.6	1.0	N_2	-
TNP0.5	−43.1 ± 1.2	0.5	-	-
TPP0.5	+53.9 ± 0.6	0.5	-	-
TNP0.5-N_2	−43.1 ± 1.2	0.5	N_2	-
TPP0.5-N_2	+53.9 ± 0.6	0.5	N_2	-
TNP0.5-Air	−43.1 ± 1.2	0.5	Air	-
TPP0.5-Air	+53.9 ± 0.6	0.5	Air	-
TNP0.5-N_2-Air	−43.1 ± 1.2	0.5	N_2	Air
TPP0.5-N_2-Air	+53.9 ± 0.6	0.5	N_2	Air

[a]Zeta potential of TWC NPs is +53.3 ± 0.8 mV.

Characterization

The Zeta potentials of the TWC NPs and PMMA particles were measured using a dynamic light scattering device (Zetasizer Nano ZSP, Malvern Instruments Ltd., Malvern, UK). The remaining PMMA in the TWC particles was analyzed by thermogravimetric analysis (TGA; TGA-

50/51, Shimadzu Corp., Kyoto, Japan) in air at an increasing temperature rate of 10°C/min. The morphologies of the samples were observed by field-emission scanning electron microscopy (FE-SEM; S-5200, 1–5 kV, Hitachi Corp., Japan). The SEM image was used to obtain the average size of the particles by measuring 300 particles using the ImageJ software. The inner structures of the final particles were observed by transmission electron microscopy (TEM; JEM-2010, 200 kV, JEOL Corp., Japan). The crystal structure of the prepared samples were investigated by X-ray diffraction (XRD; D2 PHASER, Bruker Corp., Billerica, MA, USA). The specific surface area (SSA) and pore characteristics of the mesopores and macropores of the particles were investigated using N_2 adsorption–desorption isotherm, measured by using BELSORP-max (Microtract BEL, Japan) at 77 K following the Brunauer–Emmett–Teller, Barrett–Joyner–Halenda (BJH), and *t*-plot method (for micropores).[23] Prior to these analyses, all the samples were outgassed at 110°C for 6 h under vacuum conditions to remove moisture and other volatile compounds.

Catalytic performance evaluation

Figure 1c shows the apparatus setup for evaluating the catalytic performance of the particles for CO and soot particle oxidations. To evaluate the CO oxidation performance, the nanostructured TWC particles (4.55 mg) were placed in a quartz tube (inner diameter = 3.8 mm). The prepared sample was sandwiched with a layer of quartz wool to ensure stable packing and pretreated by introducing N_2 gas, followed by a mixture of $CO/O_2/N_2$ (0.80/0.80/98.40 vol%), controlled using mass flow controllers. The gas was fed into the catalyst at a rate of 50 mL/min and 200°C for 30 min each time. During the measurement, the mixture gas was used to investigate the CO oxidation performance, whereas the furnace temperature was set to a range of 50°C–200°C. The CO conversion was calculated using **Equation 1**[22]:

$$\text{CO conversion}\,[\%] = \frac{\text{CO}_{\text{in}} - \text{CO}_{\text{out}}}{\text{CO}_{\text{in}}} \times 100\%. \quad (1)$$

Where CO_{in} and CO_{out} represent the peak area of CO molecules (mol) measured by gas chromatograph (GC-14B, Shimadzu, Japan) at the inlet and outlet of the catalyst bed, respectively.

To investigate the soot particle oxidation performance, a sample (10 mg) comprising soot particles (0.45 mg), nanostructured TWC particles (4.55 mg), and silica sand (5 mg). This sample was prepared under loose contact conditions, which was placed in a quartz tube for each test. A gas mixture of N_2 and O_2 (concentrations of 95% and 5%, respectively) was fed into the tube at a flow rate of 50 mL/min, controlled using mass flow controllers. The temperatures of 650°C and 700°C in the quartz tube were controlled using a programmable proportional integral derivative temperature controller. The mixture of the outlet gas was analyzed using a gas chromatograph, equipped with a thermal conductivity detector and PorapakQ 50/80 2.0 m and MA-5A 50/80 3.0 m columns (column temperature = 60°C). The CO_2 formation was calculated using **Equation 2**[23]:

$$\text{CO}_2[\text{mL/min}] = \%\text{CO}_2 \text{ in the outlet gas} \times \text{gas flow rate}. \quad (2)$$

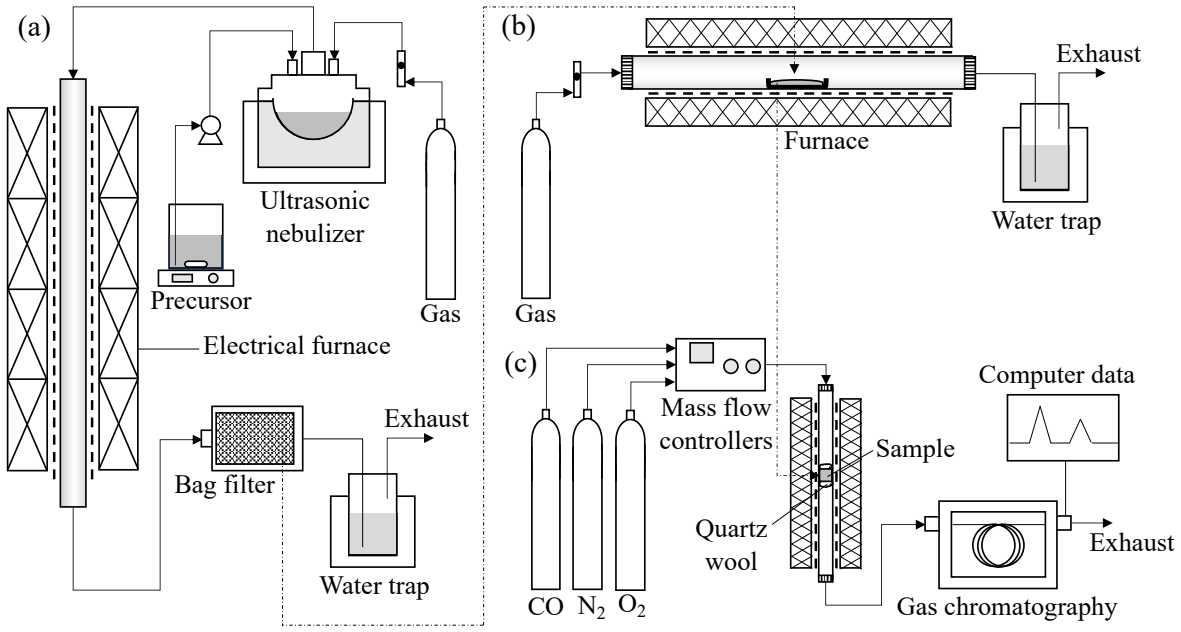

Figure 1. Experimental setup of (a) spray pyrolysis process, (b) reheating using a furnace, and (c) catalytic evaluation by gas chromatography.

RESULTS AND DISCUSSION

Synthesized particle characteristics

Figure 2 shows the SEM images of the samples prepared at a PMMA and TWC mass ratio of 1 prior to the reheating process. TNP1.0 (**Figure 2a**) and TPP1.0 (**Figure 2c**) were spherical with the remaining PMMA. For negatively charged PMMA particles, the remaining PMMA of the TNP1.0 sample was not visible on the surface of the particles (**Figure 2b**) due to that remaining PMMA in this sample was covered by TWC NPs. For the positively charged PMMA particles in the TPP1.0 sample, the remaining PMMA with an exposed surface was observed on the surface of the particles (**Figure 2d**). The TPP1.0 particles had a framework around the PMMA constructed from TWC NPs. Based on these results, the TWC particles contained the remaining PMMA that did not completely decompose during the spray pyrolysis. Thus, a reheating process was required to remove the remaining PMMA from the TWC particles.

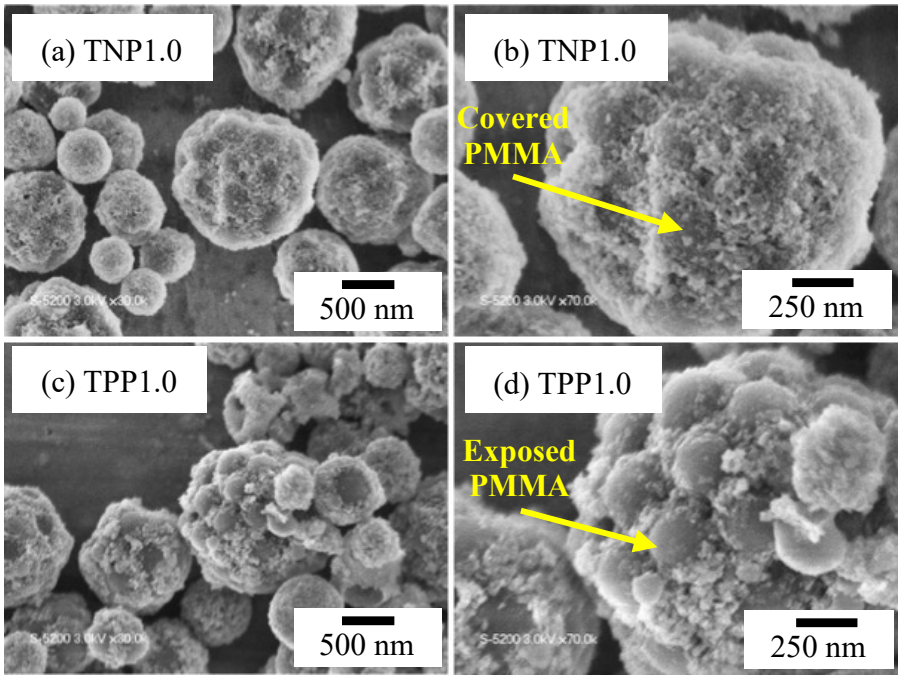

Figure 2. SEM images of TWC particles from (a and b) negatively and (c and d) positively charged PMMA with a PMMA and TWC mass ratio of 1 at (a and c) low and (b and d) high magnifications prior to reheating.

A reheating process was performed in N_2 at 900°C for 1 h to remove the remaining PMMA from the TWC particles. **Figure 3a** (TNP1.0-N_2) and **Figure 3c** (TPP1.0-N_2) show that the spherical shape of the particles was maintained after reheating. In TNP1.0-N_2, the particles derived from the negatively charged PMMA particles tended to form particles with closed pores (**Figure 3b**). Conversely, after the remaining positively charged PMMA was removed, TPP1.0-N_2 exhibited large spherical open pores that were evenly distributed on the surface of the particles (**Figure 3d**). Simultaneously, connected pores were observed in this sample. Furthermore, in the

TPP1.0-N_2 particles, the spherical pores were formed as a result of the spherical shape of the PMMA. At this point, two types of TWC particle structures (e.g., closed and open pores) were produced using PMMA with different surface charges. However, several particles in TNP1.0-N_2 exhibited open pores after reheating (**Figure 3a**). These open pores were formed because the layer of TWC NPs covering the negatively charged PMMA particles broke when the negatively charged PMMA decomposed during reheating. Owing to the presence of several particles with open pores, the catalytic performances of the two structure types were not comparable. Thus, optimal synthesis conditions for obtaining TWC particles with well-closed pores from negatively charged PMMA particles are required.

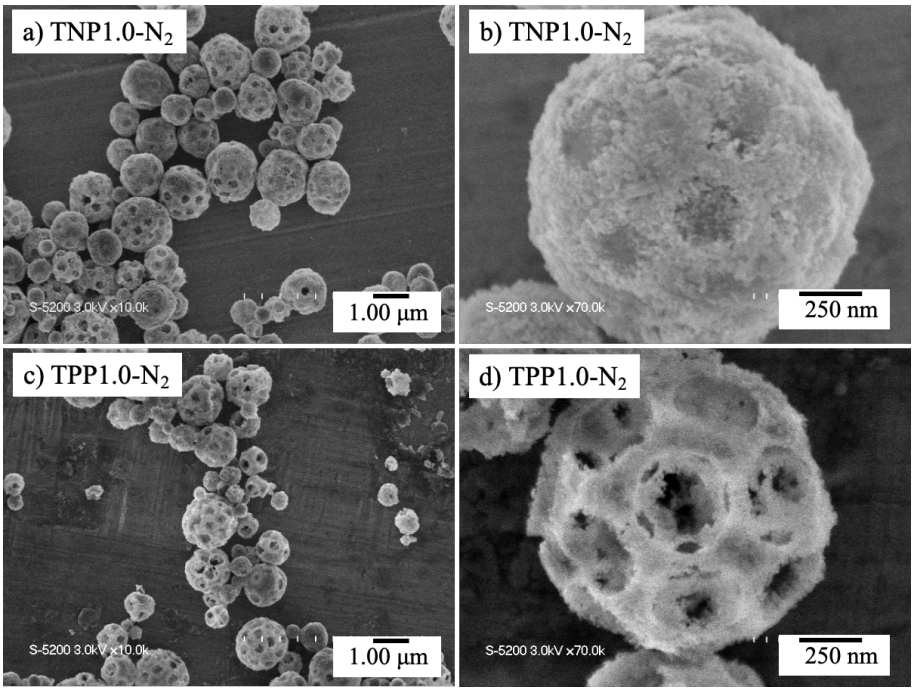

Figure 3. SEM images of TWC particles from (a and b) negatively and (c and d) positively charged PMMA with a PMMA and TWC mass ratio of 1 at (a and c) low and (b and d) high magnifications after reheating in N_2 at 900°C.

As previously mentioned, before reheating, the remaining negatively charged PMMA particles were covered by TWC NPs. However, at a PMMA and TWC mass ratio of 1, the amount of TWC NPs was too low to form a sufficiently strong cover layer on the surface of the negatively charged PMMA particles. When the reheating process to decompose the remaining PMMA was conducted, some of the cover layers of TWC NPs broke. Thereafter, several open-pore structures formed after the remaining PMMA was removed. To overcome this problem, the TWC concentration was increased to 2 wt%. The SEM images in **Figure 4a** show that the particles from TNP0.5 were spherical with the remaining negatively charged PMMA particles covered by the TWC NPs, similar to TNP1.0. The morphology of TPP0.5 (**Figure 4d**) showed results consistent with those of TPP1.0. When positively charged PMMA particles were used, the remaining PMMA with an exposed surface was exhibited on the surface of the particles. These results corresponded with the TGA curve in **Figure 4g**. Prior to reheating, a fairly large weight loss was observed within a temperature range of 300°C–500°C in TNP0.5 and TPP0.5. This weight loss indicated the presence of a large amount of PMMA in the samples that could not completely decompose during the spray pyrolysis owing to a short time in the reactor. After reheating in N_2 at 900°C for 1 h, the particles from TNP0.5-N_2 exhibited a well-closed pore (**Figure 4b**). When the TWC concentration was increased to 2.0 wt%, the amount of TWC NPs covering the negatively charged PMMA particles increased. These TWC NPs formed a sufficiently strong cover layer on the negatively charged PMMA surface. Thus, the closed pore can be maintained after reheating in N_2 at 900°C for 1 h. Conversely, large spherical open pores were uniformly distributed throughout the particle surface of TPP0.5-N_2 (**Figure 4e**). The first reheating step in N_2 was performed to slowly decompose the remaining PMMA to prevent the desired structure from damage, particularly closed-pore particles. However, several amounts of PMMA remained in the TWC particles even

after reheating in N_2 at 900°C for 1 h. As shown in the TGA results (**Figure 4g**), a weight loss occurred in TNP0.5-N_2 and TPP0.5-N_2 within 300°C–500°C, indicating that PMMA remained in the samples even after the first reheating process. However, when the reheating process in air was directly performed in the first step, several particles in TNP0.5-air exhibited open pores after the reheating process (**Figure S3a**). These open pores were formed because of the rapid decomposition of the remaining PMMA during the reheating process in air. The TWC NPs layer covering the negatively charged PMMA particles broke, resulting in several open-pore TWC particles. This result can also render their catalytic performances not comparable although TWC particles with open pores from TNP0.5-air were directly obtained (**Figure S3b**). Thus, two reheating steps (in N_2, followed by air) were performed to completely remove the remaining PMMA. **Figure 4c** shows that the particles from TNP0.5-N_2-air maintained the closed pore after the second heating step in air at 900°C for 4 h. After this reheating process, the TGA results revealed no further weight loss within 300°C–500°C for TNP0.5-N_2-air and TPP0.5-N_2-air (**Figure 4g**). This result indicated that PMMA had been completely removed from the TWC particles. The particles with the framework and large spherical open pores from TPP0.5-N_2-air were also maintained (**Figure 4f**). According to the SEM image, these particles had open and connected pores, similar to TPP1.0-N_2. Thus, the synthesis conditions at a PMMA and TWC mass ratio of 0.5 and two reheating steps were suitable for producing TWC particles with closed and open pores.

The inner structures of TNP0.5-N_2-air and TPP0.5-N_2-air were observed by TEM. **Figure 4h** confirmed that the closed pores, covered by the TWC NPs layer, were produced in the TWC particles from TNP0.5-N_2-air after PMMA was removed. **Figure 4i** shows that the particles from TPP0.5-N_2-air had open pores. The SEM and TEM results can be used as a basis for categorizing the final particle structure. For TNP0.5-N_2-air, the characteristic particle structure with closed

pores covered by a thin layer of TWC NPs was classified as hollow.[24] Oppositely, particles from TPP0.5-N_2-air with pores on their surface were classified as porous.[25] The characteristics and performance of the hollow and porous TWC particles from TNP0.5-N_2-air and TPP0.5-N_2-air, respectively, were further investigated.

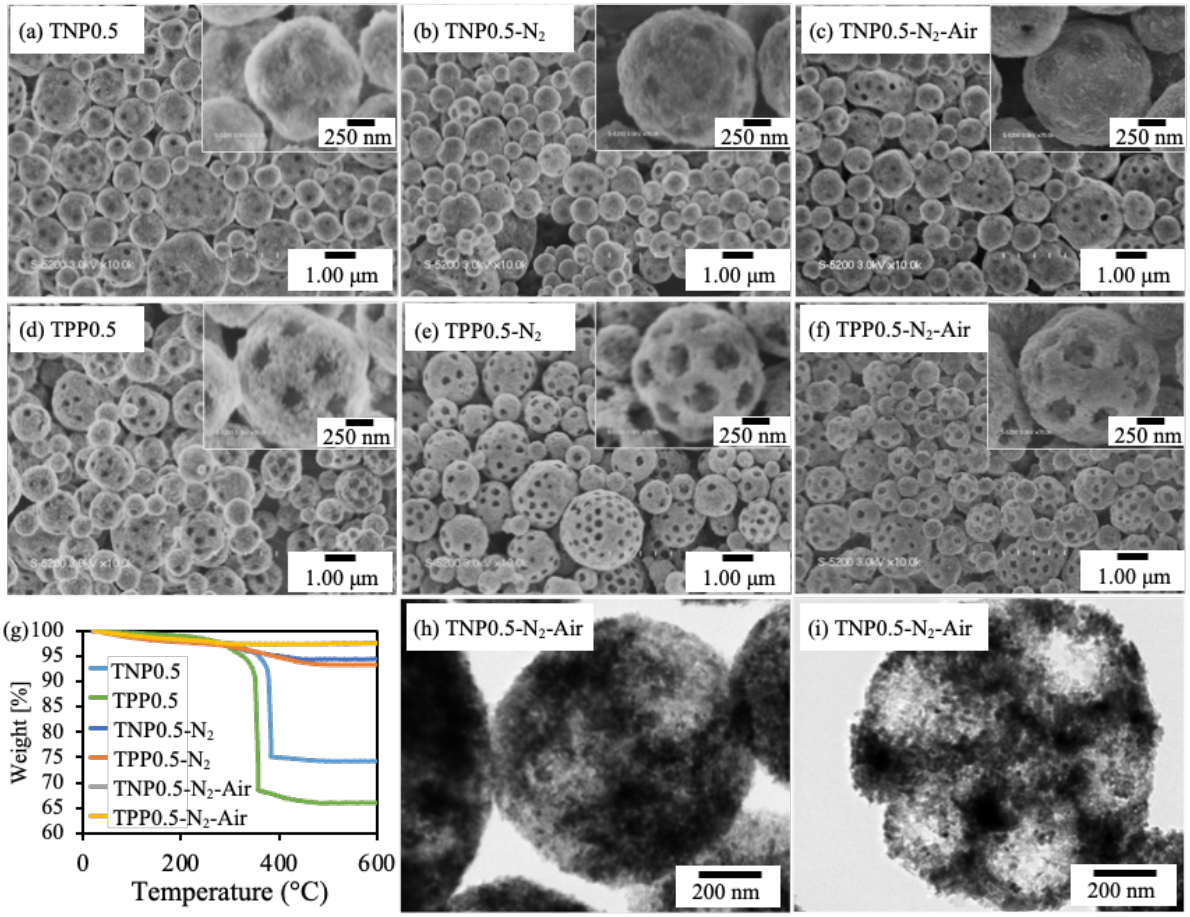

Figure 4. (a–f) SEM images, (g) TGA curves, and (h and i) TEM images of TWC particles. TWC particles prepared from template PMMA with (a–c and h) negatively and (d–f and i) positively charged particles at a PMMA and TWC mass ratio of 0.5 (a and d) prior to and (b, c, e, f, h and i) after reheating. (b and e) After the first reheating in N_2 and (c, f, h, and i) after the second reheating in air at 900°C.

Based on the aforementioned results, the proposed formation mechanism of hollow and porous TWC particles is shown in **Figure 5**. Primarily, the TWC NPs with a positive surface charge of +53.3 ± 0.8 mV were mixed with negatively and positively charged PMMA with surface charges of −43.1 ± 1.2 and +53.9 ± 0.6 mV, respectively. These precursors were atomized into spherical droplets using an ultrasonic nebulizer. When the droplets contained PMMA particles and TWC NPs with different surface charges, attractive interactions between PMMA particles and TWC NPs were occurred. Negatively charged PMMA particles attracted TWC NPs, causing the TWC NPs to attach to the surface of the PMMA particles. When the amount of TWC NPs in the droplet was sufficiently high to cover the entire surface of the PMMA particles, a core-shell-like structure was formed. As solvent evaporation and droplet shrinkage occur, the core-shell-like structure was compacted into spherical PMMA–TWC composite particles[24,26]. After the reheating process, the PMMA is removed, leaving closed pores on the final particle as hollow TWC particles. Conversely, repulsive interactions occurred when PMMA particles and TWC NPs with the same surface charge were present in the droplet. The repulsive electrostatic force caused the PMMA particles and TWC NPs to move individually. During drying, PMMA particles, which are larger, move slower to the droplet periphery than TWC NPs owing to the capillary forces as the solvent evaporates.[27] Considering the Brownian motion of the particles, TWC NPs can easily move and rotate from one place to another because the smaller particles of TWC NPs exhibit a higher Brownian motion effect than the larger PMMA particles.[28] Thus, although TWC NPs can move and arrange in the droplet periphery first, the larger PMMA particles can easily shift the arrangement to form equilibrium configurations. As the solvent continuously evaporated, the droplet gradually shrunk, causing a narrowing of the droplet periphery. At this point, the PMMA particles and TWC NPs were forced to the droplet center. Considering that this force was stronger

than the repulsive force arising from colloidal interactions, the surfaces of the PMMA particles were in contact with each other.[26] The interaction between the PMMA particle surfaces created a large void in certain parts of the droplet. Considering that TWC NPs can easily move, the large void was filled by TWC NPs. During this step, the PMMA particles and TWC NPs were arranged in the composite aggregate structure.[29,30] After all the solvents had evaporated, composite particles with exposed PMMA surfaces and thick frameworks were obtained. PMMA removal by reheating led to the decomposition of PMMA. The decomposition of PMMA with exposed surfaces left open pores on the surface of the TWC particles. Finally, particles with open pores on the surface were obtained, namely porous TWC particles. Furthermore, the differences in the particle self-assembly behavior from precursor components influenced the formation of thicker frameworks and connected pores. As previously mentioned, the electrostatic repulsion between negatively charged PMMA and TWC particles led to the formation of composite particles where PMMA particles were exposed and in contact at the interface. Thus, TWC NPs filled the voids around the PMMA, thereby forming a thicker framework. Connected pores were formed in the porous TWC particles after the decomposition of PMMA. For the hollow structure, the formation of a core-shell-like structure from precursor components prevented the PMMA particles from contacting each other. Consequently, the TWC NPs were distributed on the surface of PMMA particles, resulting in a thin framework. After the PMMA removal process, TWC particles without connected pores were formed.

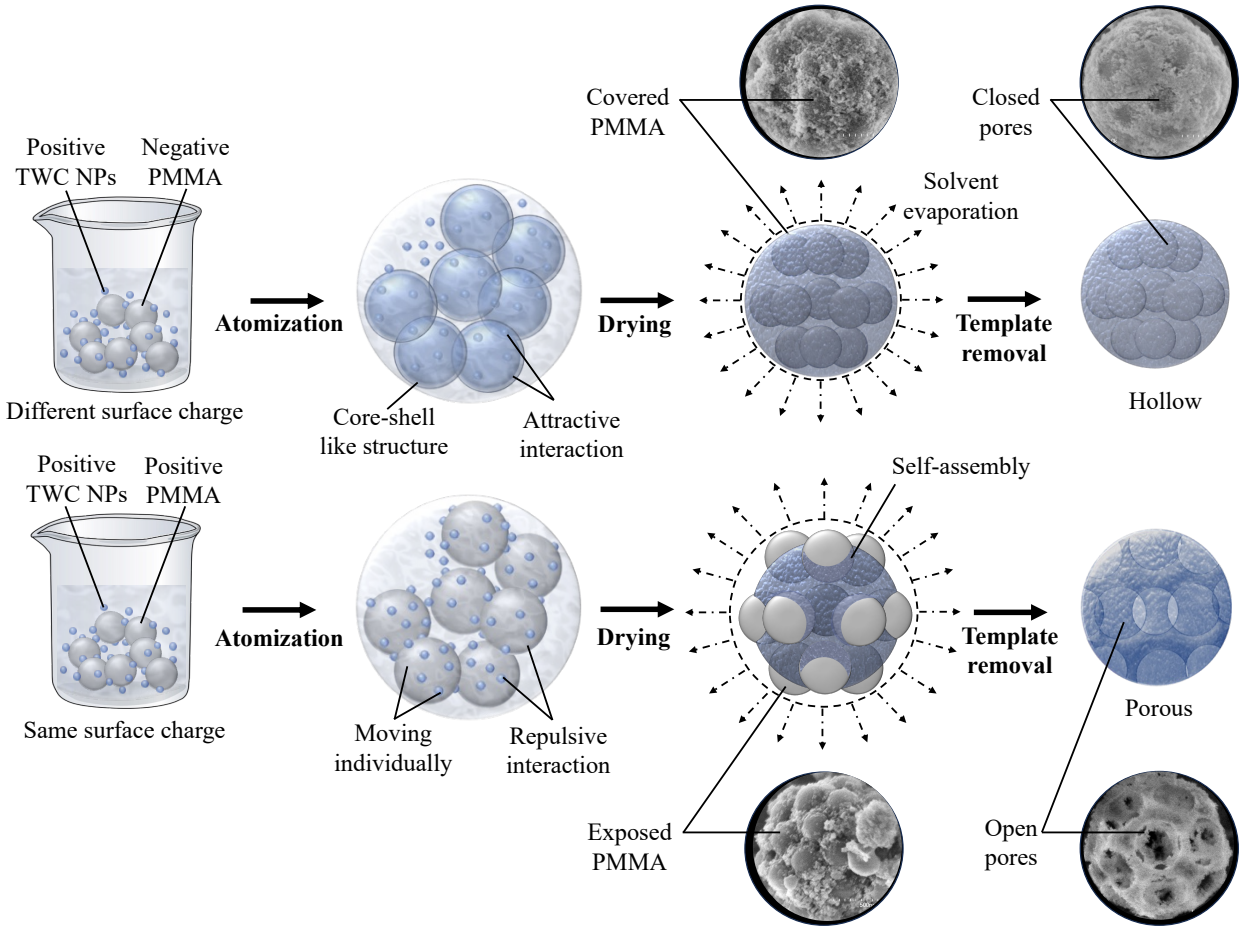

Figure 5. Formation mechanism of hollow and porous TWC particles.

The crystal structure of TWC particles from TNP0.5-N_2-air and TPP0.5-N_2-air were investigated by XRD. **Figure 6a** shows the XRD patterns of the TWC NPs, TNP0.5-N_2-air, and TPP0.5-N_2-air samples. According to 2θ from 20° to 80°, the TWC NPs comprised $CeZrO_4$ and Al_2O_3. The same prominent diffraction patterns of TNP0.5-N_2-air and TPP0.5-N_2-air confirmed that they had the same crystal structure as the TWC NPs. The patterns of TWC particles from TNP0.5-N_2-air and TPP0.5-N_2-air did not change during the synthesis process, indicating that TWC possessed good thermal stability properties. Furthermore, in the TWC particles, $CeZrO_4$ functioned as an oxygen storage component, whereas Al_2O_3 improved the thermal stability properties. N_2 adsorption–desorption analysis was employed to assess the structural properties of

the obtained TWC particles (**Figure 6b**). According to the International Union of Pure and Applied Chemistry, the similar isotherm curves of TWC particles from TNP0.5-N_2-air and TPP0.5-N_2-air were type-II isotherm curves. The presence of a hysteresis loop at a relative pressure above 0.7 was classified as H2 hysteresis.[17] These characteristics corresponded with the presence of macropores.[31] In addition, the isotherm curves showed a significant increase in the quantity of adsorbed nitrogen gas at the beginning of an increase in relative pressure, followed by a gradual increase. This phenomenon was attributed to the presence of mesopores.[32,33] The existence of macropore structures was caused by the decomposition of PMMA, and the formation of mesopores was related to the aggregation of TWC NPs in the particle framework.[20] The pore-size distribution curve of TPP0.5-N_2-air was similar to that of TNP0.5-N_2-air (**Figure 6c**), and both samples comprised mesopores. The curves showed that the pore-size distribution of macropores was low for both samples. This result was due to the limitations of the BJH method in measuring macropores. The presence of micropores in the TWC particles from TNP0.5-N_2-air and TPP0.5-N_2-air was investigated by the *t*-plot method. **Figures 6d and e** show that both samples exhibited similar regimes. The initial regime can be fitted with a straight line through the origin. The intercept of this line provides an estimate of the microporous volume. However, the intercept line of both samples points to the y-axis at 0. This result confirmed that there was no micropore formation in the TWC particles from TNP0.5-N_2-air and TPP0.5-N_2-air.[34] The absence of micropores in the TWC particles corresponded to the TWC NPs that were not micropores.

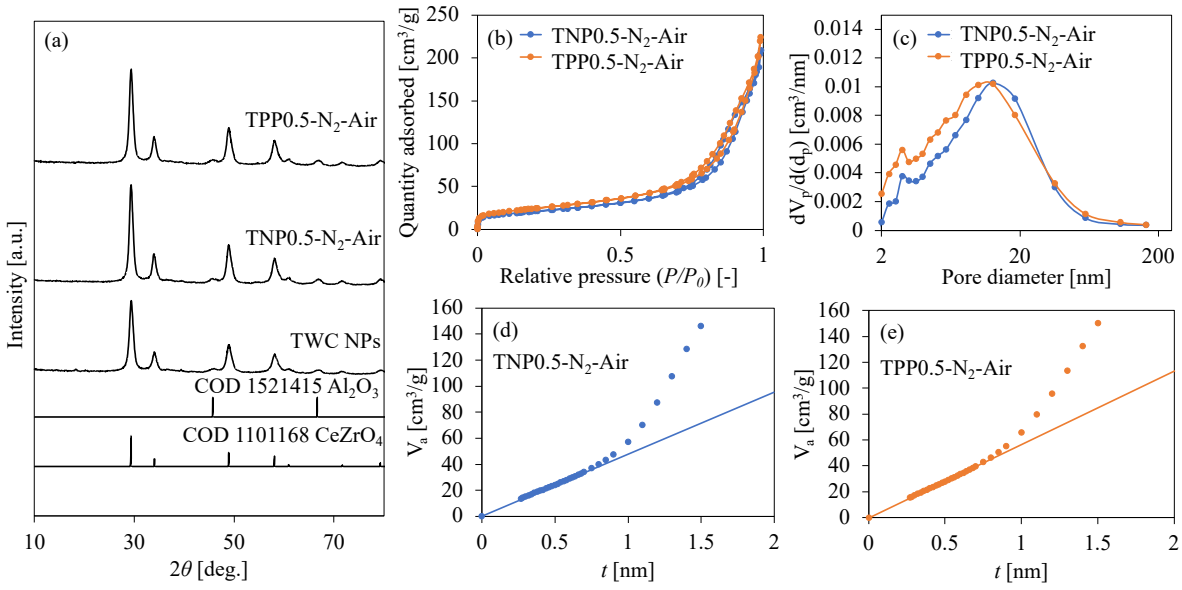

Figure 6. (a) XRD patterns, (b) N_2 adsorption–desorption isotherms, and (c) pore-size distributions of TWC particles. (d and e) *t*-curves of TWC particles from (d) negatively and (e) positively charged PMMA after the second reheating step.

Table 2 lists the measurements of the SSA, pore volume, and particle size of TNP0.5-N_2-air and TPP0.5-N_2-air after the second reheating step. The difference in the SSAs of the hollow TWC particles from TNP0.5-N_2-air and porous TWC particles from TPP0.5-N_2-air was below 15%, and both samples had similar volumes of mesopores. These mesopores contributed to the SSA. Thus, both samples had a SSA difference below 15% due to the similar mesopore volumes. TNP0.5-N_2-air and TPP0.5-N_2-air had particle sizes of 911 and 955 nm. According to the particle-size distributions (**Figure S4**), a decrease in the particle size was observed during the reheating process. The particle sizes of TNP0.5 and TPP0.5 decreased from 1002 and 1043 nm, respectively, to 972 and 1018 nm and decreased again to 911 and 955 nm after further heating in N_2 and air. Owing to the good thermal stability properties of the TWC particles, the reduction in particle size was less than 10%. Here, large differences between the particles of TNP0.5-N_2-air and TPP0.5-N_2-air were

avoided to compare the catalytic performance based only on the particle structure of the hollow and porous TWC particles. Although differences existed in the final particle size, the difference was not significant (only 5%). Thus, the impact of these insignificant size differences was negligible on catalytic performance.

Table 2. Physical properties of hollow and porous TWC.

Sample	SSA [m^2/g]	$V_{mesopore}$ [cm^3/g]	Particle size [nm]
TNP0.5-N_2-air	74.7	0.265	911
TPP0.5-N_2-air	87.6	0.283	955

Catalytic performance

TWCs are used in exhaust gas purification filters to oxidize harmful emissions into CO_2. The harmful emissions mostly comprise gases (CO, NO_x, hydrocarbon) and solid (soot particles) substances. In this study, a preliminary experiment on the CO and soot particle oxidation reaction was conducted to investigate the catalytic performance of TWC particles with diverse structures. For the CO oxidation performance, **Figure 7a** shows that TNP0.5-N_2-air demonstrated a catalytic performance similar to that of TPP0.5-N_2-air. The gaseous emission CO was smaller than the mesopores of the TWC particles. This condition enabled CO to penetrate even the closed pores of hollow TWC. Thus, the CO gas penetrated the hollow and porous structures, resulting in a similar CO conversion performance. Internal combustion engine emissions also comprise soot particles, which originate from carbon solidification combustion that must be oxidized.[35–40] During oxidation, soot particles react with O_2 to produce CO_2. Thus, the effectiveness of the hollow and porous TWC particles in oxidizing soot particles was evaluated by measuring the rate of CO_2 formation, which served as an expression of their catalytic performance. The rate of CO_2 formation

from the samples without TWC particles was measured as a control. **Figure 7b** shows that none of the samples formed CO_2 at 650°C. When the temperature increased to 700°C, CO_2 began to form in TNP0.5-N_2-air and TPP0.5-N_2-air. The higher CO_2 formation rate of 0.128 mL/min was achieved by porous TWC particles from TPP0.5-N_2-air. The hollow TWC particles from TNP0.5-N_2-air exhibited a lower CO_2 formation rate of 0.095 mL/min, whereas the sample without TWC did not form CO_2 at this temperature. Thus, porous TWC particles exhibited a superior oxidation ability toward solid reactant soot particles. For a solid reactant, the contact area between the solid reactant and catalyst is an important factor during oxidation.[41] To better understand the contact area between soot and TWC particles, the morphology of all the samples was observed by SEM. The soot particles used here were primary spherical particles (average size = 42 nm) (**Figure S5**). When mixed with porous TWC particles from TPP0.5-N_2-air, soot particles were found on the frameworks and in the pores of the TWC particles (**Figures 7c and e**). Under this condition, the porous TWC demonstrates a greater contact area between soot and catalyst. A larger contact area provides more active sites on the catalyst surface.[42] This increases the number of available sites for catalytic reactions to take place, thereby enhancing the overall catalytic activity. At this point, the presence of open pores can lead to more efficient utilization of the catalyst and faster reaction rates. Furthermore, mixing the soot particles with hollow TWC particles from TNP0.5-N_2-air resulted in soot particles only dispersed on the surface of the TWC particles (**Figures 7d and f**). As a result, hollow TWC particles provide lower contact area between soot and catalyst. The closed pores of hollow TWC particles also become a limiting factor to efficiently utilization of the internal side of catalyst leading to the limited active sites. Thus, porous TWC particles exhibited a higher catalytic performance than hollow TWC particles. In addition, the particle morphology was observed after soot oxidation at 700°C. Most of the soot particles had been successfully removed

from the surface of hollow TWC particles (**Figure 7h**), as well as on the framework and pores of porous TWC (**Figure 7g**). The SEM images also showed that the hollow and porous structures of TWC particles were maintained after the soot particle oxidation process.

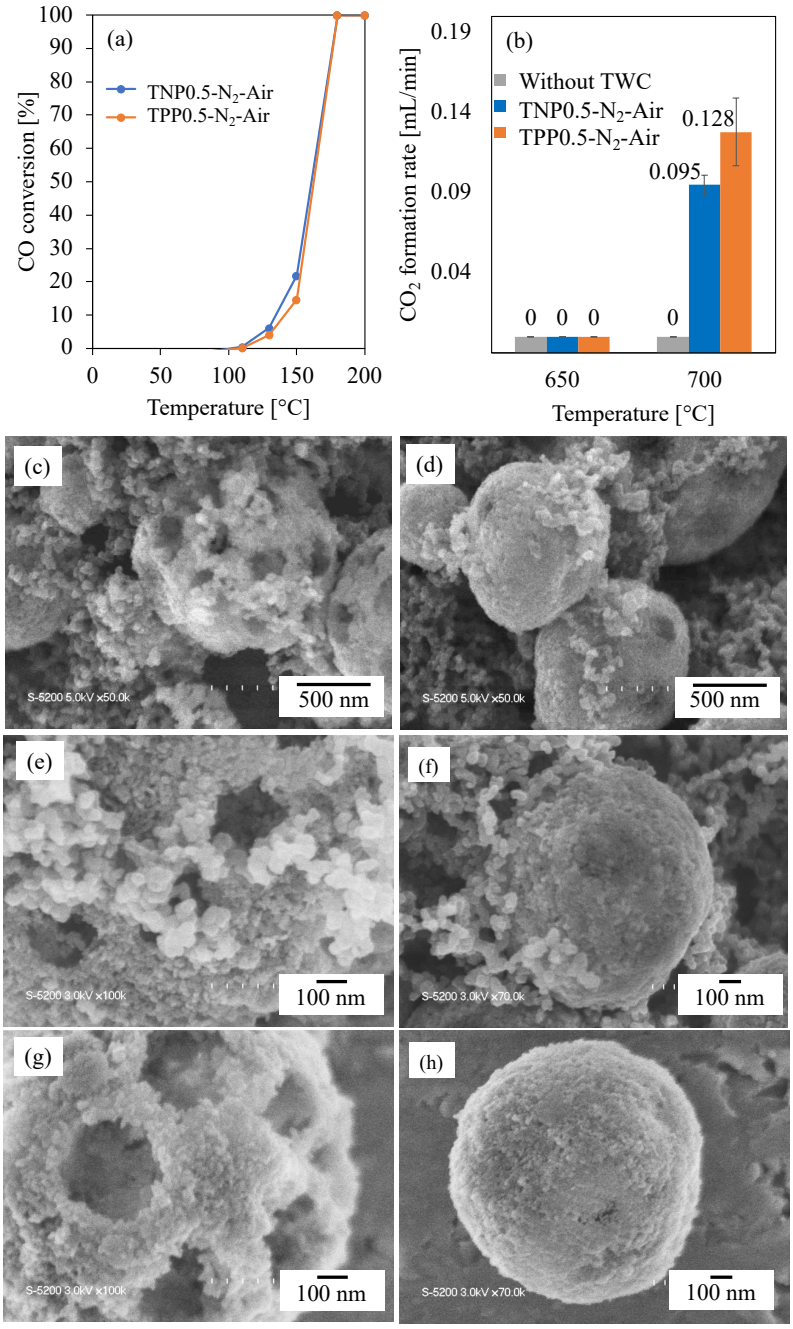

Figure 7. (a) CO conversion performance, (b) CO_2 formation rate from the investigation of soot particle oxidation performance, and (c–h) SEM images of soot particles mixed with (c, e, and g) porous and (d, f, and h) TWC particles at (c and d) low and (e–h) high magnifications. (a, c, and g) Porous and (d, f, and h) hollow structures of TWC particles (c–f) before and (g and h) after soot oxidation.

Conclusions

Nanostructured TWC particles with hollow and porous structures were prepared via a template-assisted spray pyrolysis method. Electrostatic forces between the host (TWC NPs) and template (PMMA) were used to control the structure of TWC particles. The attraction forces between negatively charged PMMA and positively charged TWCs formed hollow TWC particles. Contrarily, when the surface charge of PMMA became positive, porous TWC particles were obtained as a result of a repulsive force between the precursor components. These results showed that the surface charge properties of the materials used are important factors to consider in nanostructured TWC particles. Understanding their self-assembly behavior influenced by electrostatic forces can improve the control of the TWC particle structure. Furthermore, the catalytic performances of hollow and porous TWC particles showed no significant difference in CO conversion. This was attributed to the small size of CO gas, which allowed it to diffuse to both structures. However, during the oxidation of soot particles, the porous TWC particles exhibited a performance superior to that of the hollow TWC particles due to the higher contact area between catalysts and the solid reactant. This investigation of the catalytic performance of TWC particles for CO conversion and soot oxidation unlocks the advancement of the application of TWCs by introducing porous structures.

ASSOCIATED CONTENT

Supporting Information

The following file is available free of charge.

Surface charge modification of PMMA particles; Morphology of TWC NPs, PMMA, TWC particles after reheating in air and soot particles.

Author Contributions

The manuscript was written through the contributions of all authors. All authors have given approval to the final version of the manuscript.

Notes

The authors declare no competing financial interests.

Acknowledgement

This research was supported by JSPS KAKENHI Grant Number JP23H01745, JP22K20482, and JP23K13590. This work was also supported by JST, the establishment of university fellowships toward the creation of science and technology innovation, grant no. JPMJFS2129. This work is currently supported from a project, JPNP14004, commissioned by the New Energy and Industrial Technology Development Organization (NEDO) and the research association of Automotive Internal Combustion Engines (AICE). This work is partly supported by the International Network on Polyoxometalate Science at Hiroshima University, the JSPS Core-to-Core Program, and the Information Center of Particle Technology, Japan. We thank Dr. Makoto

Maeda of the Natural Science Center for Basic Research and Development (N-BARD) at Hiroshima University for TEM observation.

REFERENCES

(1) Nguyen, T. T.; Saipul Bahri, N. S. N.; Rahmatika, A. M.; Cao, K. L. A.; Hirano, T.; Ogi, T. Rapid Indomethacin Release from Porous Pectin Particles as a Colon-Targeted Drug Delivery System. *ACS Appl Bio Mater* **2023**, *6* (7), 2725–2737. https://doi.org/10.1021/acsabm.3c00218.

(2) Hung, C. Te; Duan, L.; Zhao, T.; Liu, L.; Xia, Y.; Liu, Y.; Qiu, P.; Wang, R.; Zhao, Z.; Li, W.; Zhao, D. Gradient Hierarchically Porous Structure for Rapid Capillary-Assisted Catalysis. *J Am Chem Soc* **2022**, *144* (13), 6091–6099. https://doi.org/10.1021/jacs.2c01444.

(3) Cao, K. L. A.; Taniguchi, S.; Nguyen, T. T.; Arif, A. F.; Iskandar, F.; Ogi, T. Precisely Tailored Synthesis of Hexagonal Hollow Silica Plate Particles and Their Polymer Nanocomposite Films with Low Refractive Index. *J Colloid Interface Sci* **2020**, *571*, 378–386. https://doi.org/10.1016/j.jcis.2020.03.064.

(4) Mcdonald, C. J.; Devon, M. J. Hollow Latex Particles: Synthesis and Applications. *Adv Colloid Interface Sci* **2002**, *99*, 181–213.

(5) Ratnasari, D.; Septiani, E. L.; Cao, K. L. A.; Hirano, T.; Okuda, N.; Matsumoto, H.; Ogi, T. Synthesis of Submicron-Sized Spherical Silica-Coated Iron Nickel Particles with Adjustable Shell Thickness via Swirler Connector-Assisted Spray Pyrolysis. *Langmuir* **2023**, *39* (39), 14063–14073. https://doi.org/10.1021/acs.langmuir.3c01900.

(6) Kalska-Szostko, B.; Wykowska, U.; Satuła, D. Magnetic Nanoparticles of Core-Shell Structure. *Colloids Surf A Physicochem Eng Asp* **2015**, *481*, 527–536. https://doi.org/10.1016/j.colsurfa.2015.05.040.

(7) Cao, K. L. A.; Iskandar, F.; Tanabe, E.; Ogi, T. Recent Advances in the Fabrication and Functionalization of Nanostructured Carbon Spheres for Energy Storage Applications. *KONA Powder and Particle Journal* **2023**, *40*, 197–218. https://doi.org/10.14356/kona.2023016.

(8) Wintzheimer, S.; Luthardt, L.; Cao, K. L. A.; Imaz, I.; Maspoch, D.; Ogi, T.; Bück, A.; Debecker, D. P.; Faustini, M.; Mandel, K. Multifunctional, Hybrid Materials Design via Spray-Drying: Much More than Just Drying. *Advanced Materials* **2023**, *35* (47), 2306648. https://doi.org/10.1002/adma.202306648.

(9) Ogi, T.; Nandiyanto, A. B. D.; Okuyama, K. Nanostructuring Strategies in Functional Fine-Particle Synthesis towards Resource and Energy Saving Applications. *Advanced Powder Technology* **2014**, *25* (1), 3–17. https://doi.org/10.1016/j.apt.2013.11.005.

(10) Bali, K.; Bak, M.; Szarka, K.; Juhász, G.; Sáfrán, G.; Pécz, B.; Mihály, J.; Mészáros, R. Controlling the Morphology of Poly(Ethyleneimine)/Gold Nanoassemblies through the Variation of pH and Electrolyte Additives. *J Mol Liq* **2021**, *322*, 114559. https://doi.org/10.1016/j.molliq.2020.114559.

(11) Balgis, R.; Widiyastuti, W.; Ogi, T.; Okuyama, K. Enhanced Electrocatalytic Activity of Pt/3D Hierarchical Bimodal Macroporous Carbon Nanospheres. *ACS Appl Mater Interfaces* **2017**, *9* (28), 23792–23799. https://doi.org/10.1021/acsami.7b05873.

(12) Balgis, R.; Arif, A. F.; Mori, T.; Ogi, T.; Okuyama, K.; Anilkumar, G. M. Morphology-dependent Electrocatalytic Activity of Nanostructured Pt/C Particles from Hybrid Aerosol–Colloid Process. *AIChE Journal* **2016**, *62* (2), 440–450. https://doi.org/10.1002/aic.15059.

(13) Balgis, R.; Anilkumar, G. M.; Sago, S.; Ogi, T.; Okuyama, K. Ultrahigh Oxygen Reduction Activity of Pt/Nitrogen-Doped Porous Carbon Microspheres Prepared via Spray-Drying. *J Power Sources* **2013**, *229*, 58–64. https://doi.org/10.1016/j.jpowsour.2012.11.143.

(14) Balgis, R.; Anilkumar, G. M.; Sago, S.; Ogi, T.; Okuyama, K. Rapid in Situ Synthesis of Spherical Microflower Pt/C Catalyst via Spray-Drying for High Performance Fuel Cell Application. *Fuel Cells* **2012**, *12* (4), 665–669. https://doi.org/10.1002/fuce.201200070.

(15) Rahmatika, A. M.; Goi, Y.; Kitamura, T.; Morita, Y.; Iskandar, F.; Ogi, T. Silica-Supported Carboxylated Cellulose Nanofibers for Effective Lysozyme Adsorption: Effect of Macropore Size. *Advanced Powder Technology* **2020**, *31* (7), 2932–2941. https://doi.org/10.1016/j.apt.2020.05.021.

(16) Rahmatika, A. M.; Goi, Y.; Kitamura, T.; Widiyastuti, W.; Ogi, T. TEMPO-Oxidized Cellulose Nanofiber (TOCN) Decorated Macroporous Silica Particles: Synthesis, Characterization, and Their Application in Protein Adsorption. *Materials Science and Engineering: C* **2019**, *105*, 110033. https://doi.org/10.1016/j.msec.2019.110033.

(17) Nguyen, T. T.; Toyoda, Y.; Saipul Bahri, N. S. N.; Rahmatika, A. M.; Cao, K. L. A.; Hirano, T.; Takahashi, K.; Goi, Y.; Morita, Y.; Watanabe, M.; Ogi, T. Tuning of Water Resistance and Protein Adsorption Capacity of Porous Cellulose Nanofiber Particles Prepared by Spray Drying with Cross-Linking Reaction. *J Colloid Interface Sci* **2023**, *630*, 134–143. https://doi.org/10.1016/j.jcis.2022.10.078.

(18) Nguyen, T. T.; Miyauchi, M.; Rahmatika, A. M.; Cao, K. L. A.; Tanabe, E.; Ogi, T. Enhanced Protein Adsorption Capacity of Macroporous Pectin Particles with High Specific Surface Area and an Interconnected Pore Network. *ACS Appl Mater Interfaces* **2022**, *14* (12), 14435–14446. https://doi.org/10.1021/acsami.1c22307.

(19) Le, P. H.; Kitamoto, Y.; Cao, K. L. A.; Hirano, T.; Tanabe, E.; Ogi, T. Synthesis of Macroporous Three-Way Catalysts via Template-Assisted Spray Process for Enhancing Mass Transfer in Gas Adsorption. *Advanced Powder Technology* **2022**, *33* (6), 103581. https://doi.org/10.1016/j.apt.2022.103581.

(20) Le, P. H.; Cao, K. L. A.; Kitamoto, Y.; Hirano, T.; Ogi, T. Designing the Macroporous Structure of Three-Way Catalyst Particles: The Influence of Template Concentration on Framework Thickness and Mass Transfer. *Langmuir* **2023**, *39* (22), 7783–7792. https://doi.org/10.1021/acs.langmuir.3c00621.

(21) Nandiyanto, A. B. D.; Ogi, T.; Wang, W.-N.; Gradon, L.; Okuyama, K. Template-Assisted Spray-Drying Method for the Fabrication of Porous Particles with Tunable Structures. *Advanced Powder Technology* **2019**, *30* (12), 2908–2924. https://doi.org/10.1016/j.apt.2019.08.037.

(22) Le, P. H.; Kitamoto, Y.; Yamashita, S.; Cao, K. L. A.; Hirano, T.; Amen, T. W. M.; Tsunoji, N.; Ogi, T. Macropore-Size Engineering toward Enhancing the Catalytic Performance of CO Oxidation over Three-Way Catalyst Particles. *ACS Appl Mater Interfaces* **2023**, *15* (46), 54073–54084. https://doi.org/10.1021/acsami.3c11489.

(23) Le, P. H.; Yamashita, S.; Cao, K. L. A.; Hirano, T.; Tsunoji, N.; Kautsar, D. B.; Ogi, T. CO Oxidation Enabled by Three-Way Catalysts Comprising Pd/Rh Nanoparticles Supported on

Al_2O_3 and $CeZrO_4$ Confined in Macroporous Polystyrene Latex Templates. *ACS Appl Nano Mater* **2023**, *6* (18), 17324–17335. https://doi.org/10.1021/acsanm.3c03954.

(24) Balgis, R.; Ogi, T.; Wang, W. N.; Anilkumar, G. M.; Sago, S.; Okuyama, K. Aerosol Synthesis of Self-Organized Nanostructured Hollow and Porous Carbon Particles Using a Dual Polymer System. *Langmuir* **2014**, *30* (38), 11257–11262. https://doi.org/10.1021/la502545d.

(25) Rahmatika, A. M.; Yuan, W.; Arif, A. F.; Balgis, R.; Miyajima, K.; Anilkumar, G. M.; Okuyama, K.; Ogi, T. Energy-Efficient Templating Method for the Industrial Production of Porous Carbon Particles by a Spray Pyrolysis Process Using Poly(Methyl Methacrylate). *Ind Eng Chem Res* **2018**, *57* (33), 11335–11341. https://doi.org/10.1021/acs.iecr.8b02564.

(26) Arif, A. F.; Chikuchi, Y.; Balgis, R.; Ogi, T.; Okuyama, K. Synthesis of Nitrogen-Functionalized Macroporous Carbon Particles: Via Spray Pyrolysis of Melamine-Resin. *RSC Adv* **2016**, *6* (86), 83421–83428. https://doi.org/10.1039/c6ra15217a.

(27) Kralchevsky, P. A.; Denkov, N. D. Capillary Forces and Structuring in Layers of Colloid Particles. *Curr Opin Colloid Interface Sci* **2001**, *6* (4), 383–401. https://doi.org/10.1016/S1359-0294(01)00105-4.

(28) Hassan, P. A.; Rana, S.; Verma, G. Making Sense of Brownian Motion: Colloid Characterization by Dynamic Light Scattering. *Langmuir* **2015**, *31* (1), 3–12. https://doi.org/10.1021/la501789z.

(29) Arutanti, O.; Nandiyanto, A. B. D.; Ogi, T.; Kim, T. O.; Okuyama, K. Influences of Porous Structurization and Pt Addition on the Improvement of Photocatalytic Performance of WO_3

Particles. *ACS Appl Mater Interfaces* **2015**, *7* (5), 3009–3017. https://doi.org/10.1021/am507935j.

(30) Nandiyanto, A. B. D.; Hagura, N.; Iskandar, F.; Okuyama, K. Design of a Highly Ordered and Uniform Porous Structure with Multisized Pores in Film and Particle Forms Using a Template-Driven Self-Assembly Technique. *Acta Mater* **2010**, *58* (1), 282–289. https://doi.org/10.1016/j.actamat.2009.09.004.

(31) Kitamoto, Y.; Cao, K. L. A.; Le, P. H.; Abdillah, O. B.; Iskandar, F.; Ogi, T. A Sustainable Approach for Preparing Porous Carbon Spheres Derived from Kraft Lignin and Sodium Hydroxide as Highly Packed Thin Film Electrode Materials. *Langmuir* **2022**, *38* (11), 3540–3552. https://doi.org/10.1021/acs.langmuir.1c03489.

(32) Balgis, R.; Ogi, T.; Arif, A. F.; Anilkumar, G. M.; Mori, T.; Okuyama, K. Morphology Control of Hierarchical Porous Carbon Particles from Phenolic Resin and Polystyrene Latex Template via Aerosol Process. *Carbon* **2015**, *84* (1), 281–289. https://doi.org/10.1016/j.carbon.2014.12.010.

(33) Cao, K. L. A.; Rahmatika, A. M.; Kitamoto, Y.; Nguyen, M. T. T.; Ogi, T. Controllable Synthesis of Spherical Carbon Particles Transition from Dense to Hollow Structure Derived from Kraft Lignin. *J Colloid Interface Sci* **2021**, *589*, 252–263. https://doi.org/10.1016/j.jcis.2020.12.077.

(34) Galarneau, A.; Villemot, F.; Rodriguez, J.; Fajula, F.; Coasne, B. Validity of the *t-plot* Method to Assess Microporosity in Hierarchical Micro/Mesoporous Materials. *Langmuir* **2014**, *30* (44), 13266–13274. https://doi.org/10.1021/la5026679.

(35) Okuyama, M.; Echigo, R.; Hanamura, K.; Yoshida, H.; Koda, M.; Koganezawa, T. Modeling of Soot Particles Growth in Fuel-Rich Premixed Flame. *Int J Heat Mass Transf* **2004**, *47* (21), 4625–4635. https://doi.org/10.1016/j.ijheatmasstransfer.2003.10.044.

(36) Mao, Q.; Kawaguchi, A. T.; Mizobata, S.; Motterlini, R.; Foresti, R.; Kitagishi, H. Sensitive Quantification of Carbon Monoxide in Vivo Reveals a Protective Role of Circulating Hemoglobin in CO Intoxication. *Commun Biol* **2021**, *4* (1), 425. https://doi.org/10.1038/s42003-021-01880-1.

(37) Xiong, J.; Wei, Y.; Zhang, Y.; Mei, X.; Wu, Q.; Zhao, Z.; Liu, J.; Wu, D.; Li, J. Facile Synthesis of 3D Ordered Macro-Mesoporous $Ce_{1-x}Zr_xO_2$ Catalysts with Enhanced Catalytic Activity for Soot Oxidation. *Catal Today* **2020**, *355*, 587–595. https://doi.org/10.1016/j.cattod.2019.05.061.

(38) Mitsouridis, M. A.; Karamitros, D.; Koltsakis, G. Model-Based Analysis of TWC-Coated Filters Performance. *Emission Control Science and Technology* **2019**, *5* (3), 238–252. https://doi.org/10.1007/s40825-019-00124-3.

(39) De Abreu Goes, J.; Woo, J. W.; Olsson, L. Effects of Feed Gas Composition on Fresh and Aged TWC-Coated GPFs Loaded with Real Soot. *Ind Eng Chem Res* **2020**, *59* (23), 10790–10803. https://doi.org/10.1021/acs.iecr.0c00654.

(40) Khaskheli, A. A.; Xu, L.; Liu, D. Manganese Oxide-Based Catalysts for Soot Oxidation: A Review on the Recent Advances and Future Directions. *Energy Fuels* **2022**, *36* (14), 7362–7381. https://doi.org/10.1021/acs.energyfuels.2c01492.

(41) Yu, Q.; Xiong, J.; Li, Z.; Mei, X.; Zhang, P.; Zhang, Y.; Wei, Y.; Zhao, Z.; Liu, J. Optimal Exposed Crystal Facets of α-Mn_2O_3 Catalysts with Enhancing Catalytic Performance for Soot Combustion. *Catal Today* **2021**, *376*, 229–238. https://doi.org/10.1016/j.cattod.2020.05.039.

(42) Sun Park, C.; Lee, M. W.; Lee, J. H.; Jeong, E. J.; Lee, S. H.; Choung, J. W.; Kim, C. H.; Ham, H. C.; Lee, K.-Y. Promoting Effect of H_2O over Macroporous Ce-Zr Catalysts in Soot Oxidation. *Molecular Catalysis* **2019**, *474*, 110416. https://doi.org/10.1016/j.mcat.2019.110416.

GRAPHICAL ABSTRACT

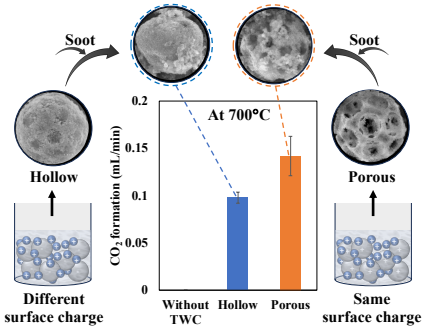

Supporting Information

Controllable synthesis of porous and hollow nanostructured catalyst particles and their soot oxidation

*Duhaul Biqal Kautsar, Phong Hoai Le, Ai Ando, Kiet Le Anh Cao, Eka Lutfi Septiani, Tomoyuki Hirano, and Takashi Ogi**

Chemical Engineering Program, Department of Advanced Science and Engineering, Graduate School of Advanced Science and Engineering, Hiroshima University, 1-4-1 Kagamiyama, Higashi-Hiroshima City, Hiroshima 739-8527, Japan

*Corresponding author: Takashi Ogi, ogit@hiroshima-u.ac.jp

Tel/Fax: +81-82-424-3765

Contents:

1. Surface charge modification of PMMA particles

The process of modifying the surface charge of PMMA involves mixing and several washings. A mixture of PMMA and CTAB at concentrations of 0.2 wt% and 0.1 M, respectively, was stirred for 24 h. Afterward, the mixture was centrifuged for 10 min and washed with water thrice.

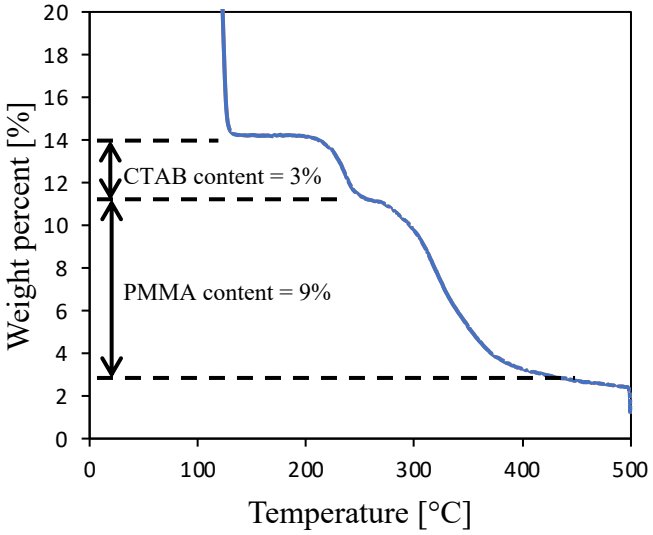

Figure S1. TGA of PMMA with positive surface charge.

2. Number ratio of TWC NPs and PMMA particles calculation

The ratio of TWC NPs to PMMA particles in one droplet is calculated using **Equation 1** obtained from previous study.[1]

$$n_{\mathrm{TWC/PMMA}} = \frac{C_{\mathrm{d-TWC}} \times \rho_{\mathrm{PMMA}} \times (D_{\mathrm{PMMA}})^3}{C_{\mathrm{d-PMMA}} \times \rho_{\mathrm{TWC}} \times (D_{\mathrm{TWC}})^3} \quad (1)$$

where $n_{\mathrm{TWC/PMMA}}$ is the number ratio of TWC NPs and PMMA particles in one droplet. $C_{\mathrm{d-TWC}}$ and $C_{\mathrm{d-PMMA}}$ are concentrations of TWC NPs and PMMA particles in solution, respectively. ρ_{TWC} and ρ_{PMMA} are densities of TWC NPs (4.83 g/cm^3) and PMMA particles (1.18 g/cm^3), respectively. D_{TWC} and D_{PMMA} are average diameters of TWC NPs (8 nm) and PMMA particles (334 nm and 368 nm), respectively.

Based on **Equation 1**, the calculated results for the number ratio of TWC NPs and PMMA particles are presented in **Table S1** as follows.

Table S1. Number ratio of TWC NPs and PMMA particles.

PMMA and TWC weight ratio [-]	**Number ratio of TWC NPs and PMMA particles [-]**	
	Negatively charged PMMA (334 nm)	**Positively charged PMMA (368 nm)**
1.0	17779	23780
0.5	35558	47560

3. Morphology of prepared samples

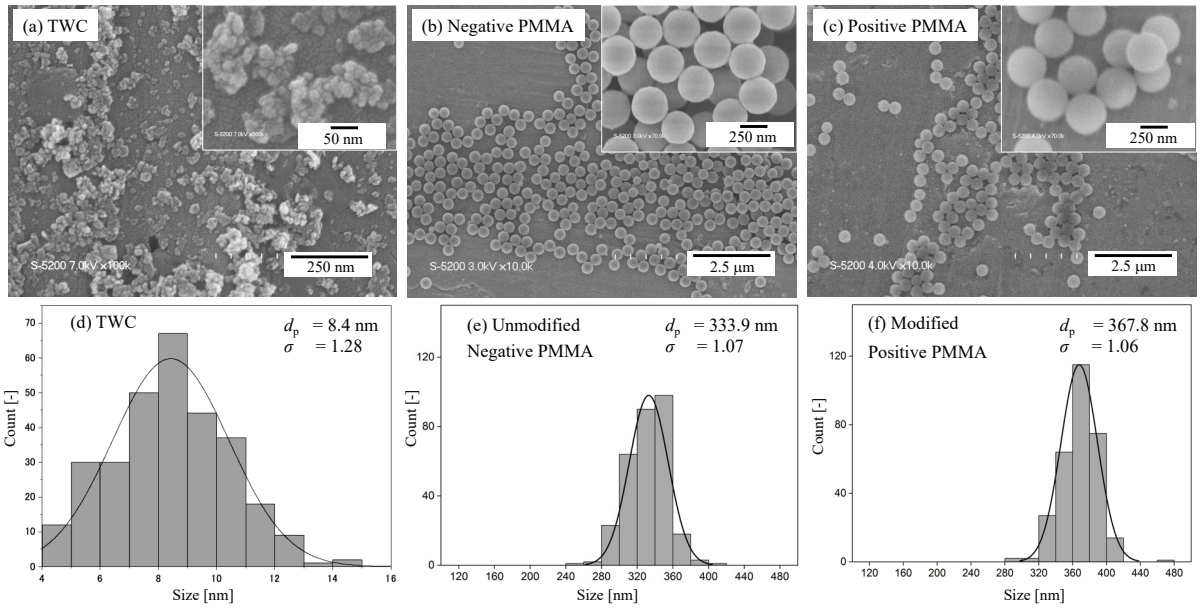

Figure S2. (a–c) SEM images and (d–f) particle-size distributions of (a and d) TWC NPs, (b and e) negatively charged PMMA particles, and (c and f) positively charged PMMA particles.

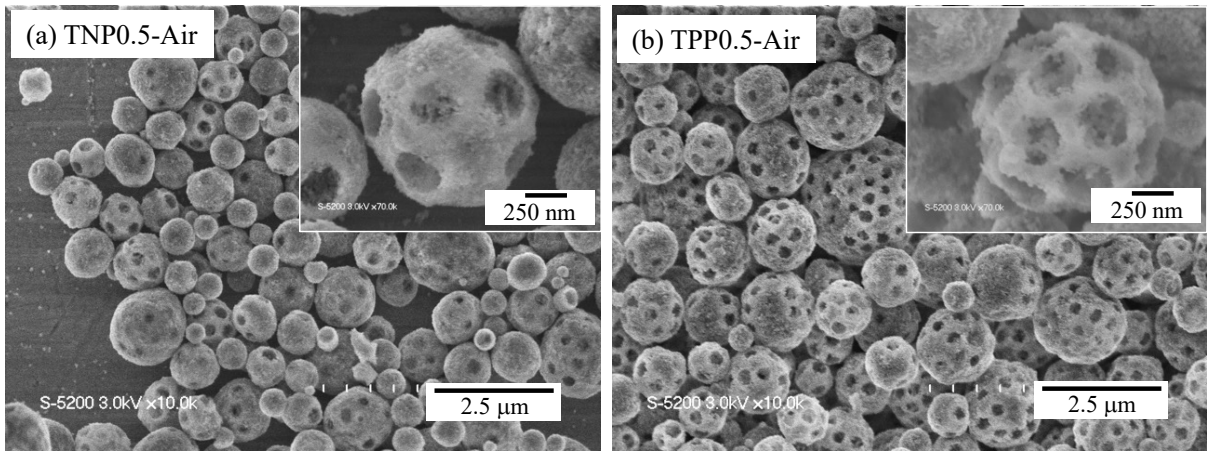

Figure S3. SEM images of TWC particles from (a) negatively and (b) positively charged PMMA particles at a PMMA and TWC mass ratio of 0.5 after reheating in air at 900°C.

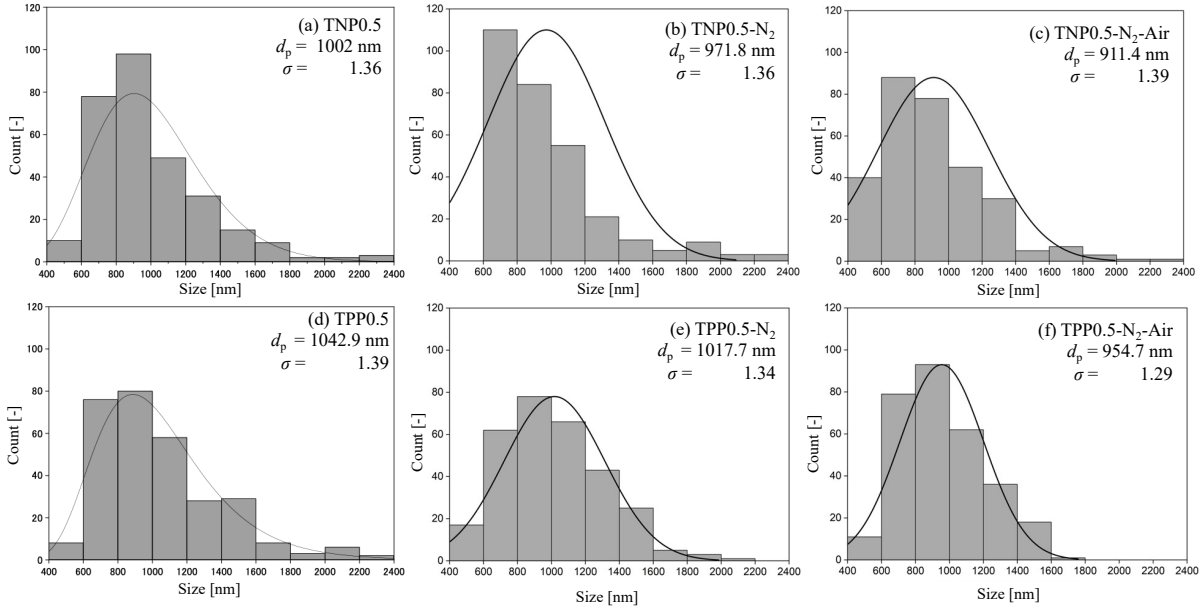

Figure S4. Particle-size distributions of TWC particles from (a–c) negatively and (d–f) positively charged PMMA particles at a PMMA and TWC mass ratio of 0.5 (a and d) before and (b, c, e, and f) after reheating in (b and e) N_2 and (c and f) N_2-air at 900°C.

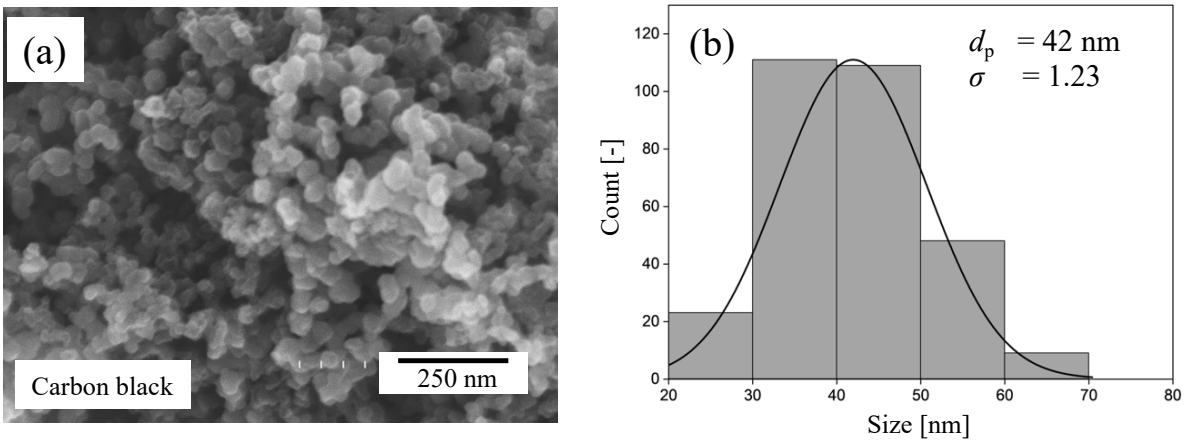

Figure S5. (a) SEM image and (b) particle-size distribution of carbon black as soot particles.

References

(1) Le, P. H.; Cao, K. L. A.; Kitamoto, Y.; Hirano, T.; Ogi, T. Designing the Macroporous Structure of Three-Way Catalyst Particles: The Influence of Template Concentration on Framework Thickness and Mass Transfer. *Langmuir* **2023**, *39* (22), 7783–7792. https://doi.org/10.1021/acs.langmuir.3c00621.